University of Dundee

Bi/SnO2/TiO2-graphene nanocomposite photocatalyst for solar visible light–induced photodegradation of pentachlorophenol

Sayadi, Mohammad Hossein; Homaeigohar, Shahin; Rezaei, Ayoob; Shekari, Hossein

Link to publication in Discovery Research Portal

1   **Bi/SnO₂/TiO₂-Graphene nanocomposite photocatalyst for solar visible light induced**

2   **photodegradation of pentachlorophenol**

3   **Mohammad Hossein Sayadi*[1], Shahin Homaeigohar[2], Ayoob Rezaei[1], Hossein Shekari[1]**

4   1: Department of Environmental Engineering, Faculty of Natural Resources and Environment, University of

5   Birjand, Birjand, Iran.

6   2: School of Science & Engineering, University of Dundee, Dundee, DD1 4HN, United Kingdom.

7   ***Corresponding author:** Mohammad Hossein Sayadi, Department of Environmental Engineering, Faculty of

8   Natural Resources and Environment, University of Birjand, Birjand, Iran

9   Tel.: +98 5632254068

10   Fax: +98 5632254066

11   Email: mh_sayadi@birjand.ac.ir

12   **Abstract:**

13   In this study, for the first time, a TiO₂/Graphene (G) heterostructure was synthesized and doped by Bi

14   and SnO₂ nanoparticles through a hydrothermal treatment. The as-synthesized nanocomposite was

15   employed for photocatalytic degradation of pentachlorophenol (PCP) under visible light irradiation.

16   Structural characterizations such as X-ray photoelectron spectroscopy (XPS) and X-ray diffraction

17   spectroscopy (XRD) proved the valence band alignment at Bi/SnO₂/TiO₂-G interfaces and

18   crystallinity of the nanocomposite, respectively. The as-developed nanocomposite photocatalyst was

19   able to decompose 84% PCP, thanks to the generation of a large number of active OH^- and $O_2^{\bullet-}$

20   radicals. To achieve this optimum photodegradation efficiency, various parameters such as pH,

21   catalyst dosage, and PCP concentration were optimized. The results showed that the PCP

22   photodegradation process followed the first-order kinetic model and the reaction rate constant rose

23   from 0.007 min⁻¹ (Bi) to 0.0149 min⁻¹ (Bi/SnO₂/TiO₂-G). The PCP photodegradation efficiency did

24   not decrease significantly after 5 cycles and the nanocomposite photocatalyst still showed a high

25   efficiency of 68% in the last cycle. The excellent photocatalytic activity of Bi/SnO₂/TiO₂-G is

26   ascribed to the novel composition as well as the heterostructure of the nanocomposite photocatalyst.

27   **Keywords**: Advanced oxidation processes; solar photocatalysis; reusability; water treatment.

28

1. Introduction

30   In the current era, by evolving industrialization and urbanization, two critical concerns of water

31   scarcity and energy resources depletion have emerged (Homaeigohar and Elbahri 2014). One

32   promising solution to tackle such challenges is development of photocatalytic nanomaterials. This

33 class of advanced materials can offer distinct merits with respect to production of H_2 and O_2 from

34 water (Kudo and Miseki 2009), reduction of CO_2 to carbon fuels (Habisreutingeret al. 2013) and

35 photodegradation of organic pollutants (Gaya and Abdullah 2008; Homaeigohar 2020). Thus, they put

36 promise for next generation of "green" technologies targeting clean energy demand and

37 environmental remediation.

38   In 1972, Fujishima and Honda for the first time found out that water is split into H_2 and O_2

39 when an immersed TiO_2 anode, connected to a Pt black cathode, is excited with an external bias. This

40 phenomenon implied that water can be photodecomposed into H_2 and O_2 in the presence of a visible

41 light provoked catalyst (Fujishima and Honda 1972). TiO_2 is indeed one of the most studied

42 photocatalysts for the purpose of water splitting and photodecomposition of organic pollutants

43 (Homaeigoharet al. 2019; S.Sh. Homaeigoharet al. 2012). Despite such versatility, it possesses a wide

44 band gap energy (3.0-3.2 eV) and thus excites photons solely in the UV light range, accounting for

45 ~4% of the solar light (Gaya and Abdullah 2008; Habisreutingeret al. 2013). Given that, the visible

46 light is largely available everywhere on the earth and accounts for ~50% of the solar light, an

47 extensive attention has been paid to development of the photocatalysts operating under visible light

48 (Ghadimiet al. 2020; Gómez-Aviléset al. 2019; Homaeigoharet al. 2017; Khanet al. 2019). Another

49 problem in relevance to TiO_2, is the possibility of fast recombination of electron-hole pairs (Chen and

50 Mao 2007).

51   Graphene has shown to be a high potential matrix able to perform as an acceptor and

52 transporter of the photogenerated electrons of TiO_2. These charge carriers can readily move via the

53 graphene nanosheets, thereby lowering the chance of fast $e^{-}-h^{+}$ recombination. Moreover, induced by

54 the presence of the negatively charged functional groups and high surface area, a large adsorption

55 capacity for the water pollutants by the graphene flakes is expected. Particularly, employing GO as

56 the matrix, a larger density of oxygen containing functional groups are available that can bring about

57 effective and fast oxidation and photodecomposition of organic pollutants (Homaeigoharet al. 2018;

58 Hu and Mi 2013). There is also a high chance for chemical bonding between d orbital in TiO_2 and π

59 orbital in graphene. Such an interaction leads to formation of a narrower band-gap thus visible light

60 photocatalytic activity for the resulting TiO$_2$/graphene nanocomposite (Kusiak-Nejman and Morawski

61 2019).

62   Despite the abovementioned merits for construction of a TiO$_2$/graphene heterostructure, light

63 harvesting efficiency of TiO$_2$ is challenged in the presence of graphene and this reduces the number of

64 the photogenerated charge carriers, thus photocatalytic activity. For the purpose of taking the most

65 advantage of solar energy and also minimizing the recombination rate of charge carriers, metal ions

66 doping is regarded as a practical supplementary approach (Ahmadpour et al. 2020; Grinberget al.

67 2019). In this regard, it has been demonstrated that some particular p-block metals are able to offer

68 orbitals that can hybridize O2p orbitals of TiO$_2$, thereby generating a more accessible hybridized

69 valence band (VB). The well-known relevant metals include Ag(I), Bi(III), and Sn(II) providing Ag

70 4d, Bi 6s, and Sn 5s orbitals, respectively, for hybridization leading to promoted mobility of

71 photogenerated charge carriers, narrowing the band gap of the photocatalyst and raising the visible

72 light absorption (Hosogiet al. 2008; Kudo and Miseki 2009). In this regard, various research groups

73 have investigated numerous relevant systems including Sn-doped TiO$_2$ nanoparticles supported onto

74 reduced graphene oxide (rGO)(Nguyen-Phanet al. 2014), Mn-doped TiO$_2$ grown on graphene (Chenet

75 al. 2016), and Bi-doped TiO$_2$ nanotube/graphene (Alamet al. 2017).

76   Here, we synthesize a TiO$_2$/graphene heterostructure, that is reinforced via metal ion doping by

77 inclusion of Bi and SnO$_2$ nanoparticles. While the former strategy, i.e. formation of a heterostructure,

78 assures a larger adsorption capacity for organic pollutants and hampers the fast recombination of the

79 charge carriers, the latter one provides a narrower band gap and enables solar visible light

80 photocatalysis. This synergetic effect is assumed to end up with the highest photocatalytic activity

81 under visible light illumination, beneficial for photodegradation of pentachlorophenol, as an organic

82 pollutant model. Pentachlorophenol has been successfully degraded by V-modified TiO$_2$ nanorod-

83 aggregates (Han et al. 2019). To the best of our knowledge, such a sophisticated composition and

84 nanostructure has not yet been reported in the literature.

85

86 **2. Materials and Methods**

87 **2.1. Materials**

88 In this study, high purity (99.5%) graphene (CAS number: 7782-42-5) was obtained from US

89 Research Nanomaterials, Inc. (3302 Twig Leaf Lane, Houston, TX 77084, USA). Sodium hydroxide,

90 bismuth nitrate, tin chloride, ammonia, ethanol, nitric acid, ethylene glycol, and tetra butyl ortho

91 titanate (TBOT) were purchased from Merck (Darmstadt, Germany). Pentachlorophenol (PCP) with

92 the chemical formula of C_6Cl_5OH was obtained from Sigma Aldrich (US).

93

94 **2.2. Sample preparation**

95 Initially, 1.07 g of Bi $(NO_3)_3 \cdot 5H_2O$ (2.2 mmol) was added to 50 mL of 0.1 mol/L mannitol solution,

96 then 20 mL $NH_3 \cdot H_2O$ (5 mol/L) was added to the solution slowly with vigorously stirring. After

97 stirring for about 30 min, the formed white precipitate was collected and washed with deionized water

98 by centrifugation for five times. The white precipitate and 0.3 g of PVP were then introduced into 50

99 mL EG. The mixture was stirred and sonicated until all the chemicals were well dispersed. Thereafter,

100 it was transferred into a stainless steel autoclave with a Teflon liner. The autoclave was sealed and

101 maintained at 180 °C for 12 h. After cooling down to room temperature, the obtained black solution

102 was centrifuged and the solid product was collected, then washed with ethanol three times and

103 eventually dried in an oven at 70 °C for 12 h (Wu et al. 2011).

104 To include SnO_2 nanoparticle, 0.3 g of Bi nanoparticle was dispersed in 30 ml deionized water and

105 sonicated (for the sonochemical process) or stirred (for the hydrothermal process). Then, 30 mL of an

106 ethanolic solution containing 1.4 g $SnCl_2$ and 1.0 g hexamine was added drop wise. This mixture was

107 sonicated for 30 min and then transferred into a Teflon stainless steel autoclave for hydrothermal

108 treatment. The autoclave was sealed, kept at 180 ° C for 12 h and allowed to cool naturally down to

109 room temperature. Finally, the precipitate was collected, washed several times with water followed by

110 absolute ethanol, and finally dried at 120 °C for 4 h. Further, it was calcinated at 500 °C for 2 h in a

111 muffle furnace fitted with a PID temperature controller (Su et al. 2012; Tang et al. 2013).

112 To synthesize $Bi/SnO_2/TiO_2$ nanoparticles, 0.35 g of Bi/SnO_2 was dispersed in 50 ml of deionized

113 water and ultrasonicated for 20 min. Subsequently, tetra butyl ortho titanate (TBOT) (4 ml) was

114 dissolved in 40 ml of ethanol and drops wise added to the Bi/SnO2-G containing suspension and

115 vigorously stirred for 2 h. The resulting mixture was transferred into an autoclave and heated at 120

116 °C for 3 h. After cooling down to room temperature, the product was centrifuged and washed several

117 times with deionized water. The precipitate was then dried in an oven for 12 h, ending up with a gray

118 powder that was $Bi/SnO_2/TiO_2$ photocatalyst (Zhu et al. 2018).

119 The synthesis of $Bi/SnO_2/TiO_2$-G was done via a hydrothermal method. 0.3 g of $Bi/SnO_2/TiO_2$

120 nanoparticles and 0.5 mg graphene nanoplatelets were added into 10 mL of absolute ethanol and

121 stirred for 10 min. The mixed solution was then sonicated for 40 min and transferred into a 25 mL

122 capacity stainless steel autoclave which was maintained at 180 °C for 12h. The resulting sample was

123 collected by centrifugation, washed with deionized water, and dried at 70 °C for 12 h.

124

125 **2.3. Structural Characterizations**

126 The crystalline structure of the nanocomposite photocatalyst was characterized by X-ray diffraction

127 (Rigaku MiniFlex 600, Japan) using Cu-Kα radiation (λ=0.15418 nm). The morphology of the

128 nanocomposite nanoparticles was investigated by using Field Emission Scanning Electron

129 Microscopy (FESEM) (TE-SCAN, MIRA3 FESEM model). X-Ray Photoelectron Spectroscopy

130 (XPS) (Thermo Scientific K-Alpha X-ray Photoelectron Spectrometer, USA) and Fourier Transform

131 Infrared Spectroscopy (FTIR) (Shimadzu, FTIR1650 spectrophotometer, Japan) were also applied to

132 determine the chemical features of the nanocomposite photocatalyst. Zeta potential measurements

133 were performed to assess zeta potential and isoelectric point of the nanoparticles using a Zetasizer

134 (3000HS) machine. Thermo gravimetry Analysis (TGA) was done using a Perkin Elmer device

135 (USA) for a temperature sweep of 50 to 800 °C under nitrogen atmosphere. The UV-Vis spectra of

136 the specimens were measured by a UV-Vis spectrophotometer (Shimadzu, UV-2550, Japan).

137

138 **2.4. UV-light Induced Photodecomposition Efficiency Analysis**

139 Batch photodecomposition experiments were performed in a 250 ml cylinder reactor containing 100

140 ml of PCP solution (30 mg/l) at room temperature. In each experiment, a certain amount of the

141 photocatalyst was added to the reactor vessel. The pH values were adjusted by addition of HCl (0.1

142 M) and NaOH (0.1 M) and controlled using a pH meter (Istek, 915PDC, Korea). At predetermined

143 intervals, 3 ml of the solution was taken, centrifuged immediately and the PCP concentration was

144 measured via high-performance liquid chromatography (HPLC) (Agilent Technologies, Infinity1260,

145 USA). An air pump (Hailea, ACO-5504, China) was attached to the set-up to homogenize the solution

146 during the experiment.

147

148 **2.5. Visible-light Induced Photodecomposition Efficiency Analysis**

149 This series of experiments was carried out inside a quartz reactor with a sunlight collector to reflect

150 light to the reactor. These experiments were performed for 2 h from 11 am to 13 pm under the

151 optimum conditions, already determined based on the UV-light induced photodegradation tests. The

152 pH of natural aquatic media lies in the neutral range. Therefore, for the current measurements based

153 on visible light irradiation, the pH value of 7 was considered. For the sake of homogenization of the

154 solution to be analyzed, an air pump was attached to the set-up.

155

156 **2.6. Photodegradation kinetics**

157 The kinetics of PCP photodegradation reactions in the presence of the Bi/SnO$_2$/TiO$_2$-G photocatalyst

158 was measured via Equation (1):

159 $$\ln\left(\frac{c}{c_0}\right) = -kt \tag{1}$$

160 *where c and* c$_0$ are the momentary and initial concentrations, respectively. k and t are the reaction

161 rate and time constants, respectively (Elmolla and Chaudhuri 2010).

162

163 **3. Results and discussion**

164 **3.1 Crystalline structure**

165 To validate the formation of the multiphasic nanocomposite photocatalyst, XRD analysis was

166 performed and the corresponding crystalline phases of each component were precisely determined.

167 Fig. 1a demonstrates the XRD pattern of G, Bi-G, Bi/SnO$_2$-G and Bi/SnO$_2$/TiO$_2$-G nanocomposites.

168 As can be seen here, graphene has three distinct peaks at 27.6°, 54.7° and 56.4°, which can be indexed

169 to (002), (004) and (110) diffraction planes, respectively (according to JCPDS-No. 75-2078). For

170 G/Bi, the characteristic peaks at 23.6° (003), 37.1° (104), 39.5° (110), 43.9° (015), 63.8° (112), and

73.7° (009) were in good agreement with the typical peaks of the rhombohedral phase of Bi (JCPDS-No. 18-0244). The diffraction peaks at $2\theta=26.71°$, $33.79°$, $54.94°$, $57.81°$, $61.96°$, and $66.03°$ correspond to (110), (101), (211), (220), (310) and (301) diffraction planes of SnO_2 core, respectively (JCPDS card No. 41-1445). The observed TiO_2 diffraction peaks at $2\theta= 25.6°$, $48.3°$, and $62.5°$ are associated with (101), (200), and (204) planes, respectively (JCPDS-No. 71-0574) (Sayadiet al. 2019). The crystallite size of the specimens was calculated via the Debye-Scherer formula (equation (2)):

$$D = \frac{k\lambda}{\beta} \cos \Theta \qquad (2)$$

where K is the grain shape factor (0.9), λ is the wavelength of X-ray (nm), d is the average crystallite size (nm), β is the full width at half max in radians and Θ is the Bragg diffraction angle of the peak in degree. According to this equation, an average crystallite size of 40 nm was measured.

3.2 Fourier Transform Infrared (FTIR) analysis

Fig. 1b shows the FT-IR spectra of the Bi/SnO_2/TiO_2-G nanocomposite. For graphene, the peaks appearing at 1060 cm^{-1}, 1372 cm^{-1}, 1635 cm^{-1}, 1726 cm^{-1}, and 3430 cm^{-1}, are attributed to the C-O stretching vibrations of epoxy groups, OH deformation vibrations of tertiary C-OH, OH deformation vibrations of COOH groups, C=O stretching of carbonyl groups and OH stretching vibrations of adsorbed water, respectively (Wanget al. 2013). The first peak located at 530 cm^{-1} and the one at 646 cm^{-1} are associated to Bi-O. The peaks located at 846 cm^{-1} and 1384 cm^{-1} are attributed to Bi-O-C and Bi-O-Bi stretching vibration, respectively (Liuet al. 2020). In the case of SnO_2, the peak emerging at about 513 cm^{-1} relates to vibrations of Sn-O. Moreover, the peaks at 463 cm^{-1} and 601 cm^{-1} can be associated to the symmetric vibrations of O-Sn-O and the asymmetric vibrations of Sn-O-Sn, respectively (Sayadiet al. 2019; Tamminaet al. 2016; Tamminaet al. 2017). Lastly, the peaks appearing at 817 cm^{-1} and 1029 cm^{-1} can be related to O-Ti-O flexural vibration and Ti-O-Ti tensile vibration, respectively (Rajakumaret al. 2014).

Fig. 1

3.3. Morphology

197   The structure and morphology of the nanocomposite photocatalyst were observed by Scanning

198   Electron Microscopy (SEM). Fig. 2a&b shows the SEM images of Bi/SnO$_2$/TiO$_2$-G samples. The

199   functionality of the graphene nanosheets results in formation of spherical Bi, SnO$_2$, and TiO$_2$

200   nanoparticles with a uniform distribution and small particle size ranging from 36 to 46 nm (Fig. 2c).

201   **Fig.2**

202

3.4 X-ray photoelectron spectroscopy (XPS) analysis

204   The surface chemistry of the Bi/SnO$_2$/TiO$_2$-G nanocomposite was examined through XPS

205   analysis. Fig. 3a shows the general XPS spectrum of Bi/SnO$_2$/TiO$_2$-G implying the existence of

206   carbon, oxygen, bismuth, tin and titanium. Fig. 3b exhibits the C1s peak of graphene wherein the

207   main peak is attributed to sp^2-hybridization (C-C bond, 284.5 eV). The three minor peaks appearing at

208   285.94, 287.51 and 288.81 eV, correspond to C-O bonds, carbonyl (C=O), and carboxylate (O-C=O)

209   functional groups, respectively (Kumaret al. 2016). Fig. 3c reveals Bi 4f peaks situated at 159.05 eV

210   and 164.29 eV, implying that Bi exists as Bi^{3+} in the composite (Jianget al. 2011). The peaks of Sn 4s,

211   3p, 4p, 3d, and 4d for SnO$_2$ are also visible in Fig. 3d. As shown in this Figure, the Sn 3d spectrum

212   includes two peaks at 487.23 and 495.67 eV that are attributable to Sn 3d$_{3/2}$ and Sn 3d$_{5/2}$ spin orbit

213   peaks of SnO$_2$, verifying the formation of SnO$_2$ nanoparticles on the surface of graphene nanosheets

214   (Kumaret al. 2015). Fig. 3e displays the TiO$_2$ spectrum, therein doublet peaks of Ti 2P$_{1/2}$ (458.63 eV)

215   and Ti 2P$_{3/2}$ (464.26 eV) are clearly seen. These peaks clarify the Ti^{4+} chemical state and imply that

216   titanium exists in the form of TiO$_2$ (Benjwal and Kar 2015).

217   **Fig. 3**

3.5 BET analysis

219 Fig. 4 shows the N$_2$ adsorption-desorption isotherms curve of Bi/SnO$_2$/TiO$_2$-G nanocomposite. From

220 the adsorption segment of the isotherm curve, the specific surface area of Bi/SnO$_2$/TiO$_2$-G

221 nanocomposite can be calculated through the multipoint Brunauer–Emmett–Teller method, as large as

222 33.38 m^2 g^{-1}. The specific surface area of Bi@SnO$_2$/TiO$_2$-G nanocomposite is mainly attributed to the

223 contribution of graphene. From the desorption segment of the isotherm curve, pore size distribution of

224 Bi/SnO$_2$/TiO$_2$-G nanocomposite can be calculated through the Barrett-Joyner-Halenda (BJH) model,

225   in the range of a typical mesoporous structure (inset). As shown here, the pores are mainly as small as

226   38.5 nm, and the total pore volume based on the pores whose size varies from 0 to 100 nm is 0. 315

227   cm^3g^{-1}.

228

229   **3.6 TGA analysis**

230   Fig. 5a shows the thermal analysis result for the $Bi/SnO_2/TiO_2$-G nanocomposite. The presence

231   of impurities remaining after a high temperature heating process on the nanocomposite photocatalyst

232   was investigated via TGA analysis. Weight losses took place in three temperature ranges of: 1) 26–

233   150°C due to the evaporation of absorbed water. 2) 250-400°C, due to the evaporation of some

234   organic precursors, and 3) 400-600°C, thereafter the nanocomposite remains stable even at

235   temperatures above 600°C.

236

237   **3.6 UV-vis DRS spectra**

238   Fig. 5b displays the UV-Vis optical absorption spectra for TiO_2, Bi, Bi/SnO_2 and $Bi/SnO_2/TiO_2$-

239   G within the wavelength range of 300-800 nm. The main absorption bands are seen in the

240   visible region for Bi (460 nm), SnO_2 (480 nm) and G (490 nm). The neat TiO_2's characteristic

241   absorption band appears at 420 nm. As other semiconductors, the band-gap energy (Eg) of the

242   photocatalysts synthesized in this study can be calculated via equation 3 (Wanget al. 2017):

243        $\alpha(hv)= A(hv - E_g)^{1/2}$ (3)

244   where E_g, hv, α and A represent the band gap energy, photon energy, absorption coefficient and

245   a constant, respectively (Huet al. 2015; Wanget al. 2017). The estimated band-gap energies of neat

246   TiO_2, Bi, Bi/SnO_2 and $Bi/SnO_2/TiO_2$-G were measured to be 3.05 eV, 2.94 eV, 2.63 eV and 2.42 eV,

247   respectively. A narrow-band gap is useful for improving the visible light absorption, thus

248    $Bi/SnO_2/TiO_2$-G can show an advanced photocatalytic performance.

249

250   **3.8 PL spectra**

251   Fig. 5c demonstrates the PL spectra of all samples in the range of 380-510 nm. Based on this figure,

252   TiO_2 shows the strongest emission, implying that the photogenerated electrons and holes are

253 recombined promptly. In contrast, the emission strength of $Bi/SnO_2/TiO_2$ and $Bi/SnO_2/TiO_2$-G is

254 lower, indicating Bi/SnO_2 and graphene can effectively separate the electron-hole pairs

255 photogenerated by TiO_2. This suggests that such a heterostructure could offer a more optimum

256 photocatalytic activity.

257

258 **3.7 Zeta potential**

259 Fig. 5d shows the variations of zeta potential in the pH range of 2 to 12 for $Bi/SnO_2/TiO_2$-G

260 nanocomposite. Based on this measurement, the zeta potential of $Bi/SnO_2/TiO_2$-G takes place at pH

261 7.3.

262 **Fig. 5**

263 **3.8 UV-light induced photodecomposition of PCP**

264 **3.8.1 Effect of pH**

265 pH notably affects pollutants' solubility and photocatalysts' surface charge and hydroxyl

266 radical production ability. Fig. 6a demonstrates the pH dependent PCP photodegradation rate of

267 $Bi/SnO_2/TiO_2$-G. When pH declines from 11 to 3, the PCP photodegradation rate increases, peaking at

268 pH3.

269 According to Fig. 6a, the highest amount of PCP degradation occurs under acidic conditions,

270 where a large concentration of H^+ ions leads to formation of many H^+ radicals. These radicals bond

271 with the oxygen present in the solution and further generate $^{\bullet}HO_2$ radicals, that can be later converted

272 to $^{\bullet}OH$ ones. Upon forming insoluble compounds at high pHs, the PCP degradation rate declines,

273 possibly due to a lower light absorption and less hydroxyl radical production (Sayadi et al. 2019).

274 Rajput et al. investigated the photodegradation process of PCP at the pH range of 3–8. Their results

275 showed that PCP degradation was affected by the solution pH and the highest degradation occurred at

276 pH3 (Rajputet al. 2018).

277

278 **3.8.2 Effect of the catalyst dosage**

279 The effect of $Bi/SnO_2/TiO_2$-G catalyst dosage on the PCP degradation rate is presented in Fig.

280 6b. Up to a certain extent, the higher the catalyst amount, the larger the PCP degradation efficiency

281 was. The reason for this observation could be related to the increased density of active sites able to

282 produce hydroxyl radicals with the catalyst dosage (Li and Shi 2016). A similar behavior has been

283 reported by Zhang et al. (Zhanget al. 2016). They declare that the extent of photodegradation of

284 phenolic compounds increases with increasing the catalyst content.

285

286 **3.8.3 Effect of the PCP initial concentration**

287   The correlation of the photodegradation rate with the PCP initial concentration is represented in

288 Fig. 6c. As shown here, the photodegradation rate decreases with increasing the PCP initial

289 concentration. This could be related to this fact that the available active sites on the photocatalyst are

290 rapidly occupied by the PCP molecules. Thus, formation of reactive radicals is hampered. Moreover,

291 at higher PCP initial concentrations, the number of photons reaching the catalyst surface and thereby

292 the photodegradation efficiency is notably reduced (Pourtaheri and Nezamzadeh-Ejhieh 2015). A

293 similar performance has also been observed by Han et al. (Hanet al. 2019).

294

295 **3.9 Comparison of PCP degradation rates by the synthesized catalysts**

296   The PCP degradation rate of Bi, Bi/SnO_2, and $Bi/SnO_2/TiO_2$-G catalysts is shown in Fig. 6d.

297 The results indicate that by changing the catalyst type from Bi to $Bi/SnO_2/TiO_2$-G a significant change

298 in the photodegradation rate (from 45% to 84%) takes place. Accordingly, $Bi/SnO_2/TiO_2$-G is

299 regarded as the most efficient catalyst for photodegradation of PCP, among the synthesized

300 compounds.

301   **Fig. 5.**

302 **3.10 The PCP photodegradation kinetics**

303   The PCP photodegradation process was analyzed from kinetics point of view. For such an

304 analysis, optimum experimental conditions including pH = 3, 20 mg/l PCP concentration, 0.3 g/l

305 catalyst (Bi, Bi/SnO_2, and $Bi/SnO_2/TiO_2$-G) concentration (dosage) and 120 min reaction time were

306 taken into account. Fig. 7a shows that the photodegradation process proceeds linearly over time and

307 complies well with the first order kinetics. Additionally, depending on the type of the catalyst, the

308 PCP photodegradation reaction rate constant rises from 0.007 min^{-1} (Bi) to 0.0149 min^{-1}

309 (Bi/SnO$_2$/TiO$_2$-G)(Table 1). Ba-Abbad et al. (Ba-Abbadet al. 2017) investigated the photocatalytic

310 degradation of PCP using ZnO nanoparticles. Their results showed that the PCP photodegradation

311 process followed the first-order kinetics and the reaction rate constant with the optimum catalyst

312 amount was 0.0052 min^{-1}.

313   **Table 1**

314 **3.11 Reusability of Bi/SnO$_2$/TiO$_2$-G**

315   Reusability of the Bi/SnO$_2$/TiO$_2$-G photocatalyst for UV-light induced photodegradation of

316 PCP was examined in five successive cycles under the optimum environmental conditions previously

317 defined. To do so, the Bi/SnO$_2$/TiO$_2$-G photocatalyst was separated from the solution after each use

318 and washed several times with deionized water; then was dried at 60°C and used again for the next

319 PCP photodegradation cycle. As shown in Fig. 7b, the PCP photodegradation efficiency did not

320 decrease significantly after 5 cycles and the nanocomposite photocatalyst still showed a high

321 efficiency of 68% in the last cycle. The reason for loss of efficiency can be associated to the

322 occupation of Bi/SnO$_2$/TiO$_2$-G surface active sites by the decomposed organic residues. Furthermore,

323 the Bi/SnO$_2$/TiO$_2$-G photocatalyst's mass declines during each cycle of the recovery process and this

324 leads to a lower PCP photodegradation efficiency (Guo et al. 2020). Overall, stability and reusability

325 of the Bi/SnO$_2$/TiO$_2$-G photocatalyst hold promise for its further application in photocatalytic

326 degradation of organic pollutants.

327   XRD was used to assess the structural properties of the catalyst before and after reuse. Fig. 7c

328 shows the XRD patterns of the catalyst before and after five cycles. As seen here, the intensity of the

329 XRD diffraction peaks negligibly declines after reuse. Therefore, no significant change is observed in

330 the XRD patterns of Bi/SnO$_2$/TiO$_2$-G before and after reuse. The peaks related to the anatase phase of

331 Ti in the XRD pattern remain almost intact even after five uses, indicating that Bi/SnO$_2$/TiO$_2$-G

332 possesses high stability and can be reused for several cycles without remarkable changes in its initial

333 crystalline structure.

334

335 **3.12 Visible light induced photodegradation of PCP by Bi/SnO$_2$/TiO$_2$-G photocatalyst**

336   As shown in Fig. 7d, the visible light induced photodegradation efficiency of Bi/SnO$_2$/TiO$_2$-G

337 photocatalyst rises over time. Comparing this performance (photodegradation rate) at two pH values

338   of 3 and 7, one can see that this catalyst has a higher degradation potential under acidic condition

339   rather than under the neutral one.

340   **Fig. 7**

341   **3.13 Visible light induced photocatalysis mechanism**

342   Scheme 1a shows the proposed reaction scheme for the visible light induced photodegradation

343   of PCP by the Bi/SnO$_2$/TiO$_2$-G nanocomposite. As seen here, graphene interlinks Bi, SnO$_2$ and TiO$_2$

344   nanoparticles, thereby causing e$^-$ and h$^+$ separation and hampering recombination. When graphene is

345   irradiated with visible light, the photogenerated electrons are shifted from valence band (VB) to

346   conduction band (CB), leaving h$^+$ in VB. On the other hand, the photogenerated electron present in

347   CB could be driven towards Bi, SnO$_2$ and TiO$_2$ through the formed junctions. A large number of O$_2$$^{\cdot-}$

348   is made over the catalyst surface through the reaction between e$^-$ and the absorbed O$_2$, that can

349   contribute to PCP degradation.

350

351   **3.14 Degradation pathways**

352   Scheme 1b proposes the possible reaction pathways for PCP photodegradation. It shows an

353   oxidative dechlorination pathway through substitution of chlorine by HO$^{\cdot}$. 14 intermediates are

354   involved in the PCP photodegradation process. The ion at m/z 265.84 represents PCP. Based on the

355   above, the photodegradation of PCP by the Bi/SnO$_2$/TiO$_2$-G nanocomposite refers to two main

356   pathways, including main product ions at m/s 247.67 and 231.92 which were identified as 2,3,5-6-

357   Tetrachloro-1,4-benzenediol (TeCP) and 2,3,5,6-Tetrachlorphenol (TCP) (Antonopoulouet al. 2014).

358   As shown in TCP pathway, during the decomposition, the reaction proceeds based on the isomers of

359   2,3,5,6-Tetrachlorphenol (TCP), 2,3,6-trichlorpheno (m/s 195.73), 2,6-dichlorophenol (m/s 162.89),

360   2,4,5-trichlorophenol (m/s 195.86) and 2,5-dichlorophenol (m/s 161.91). In another pathway, the

361   chlorination process involving 2,3,5-6-Tetrachloro-1,4-benzenediol (TeCP) results in the formation of

362   possible isomerized intermediates with m/z values of 177.82 and 143.76. Subsequently, cleavage of

363   the azo (C-Cl) bond leads to the formation of benzenoid degradation intermediates with m/z values of

364   128.42 and 93.96. This consequently gives rise to the formation of phenol, which oxidizes to form

365   maleic acid. All these aromatic intermediates would undergo further oxidation to form aliphatic

13

366 carboxylic acids (such as malonic acid). Eventually, the ring-opening reactions would give rise to

367 formation of the products that are oxidized to CO_2, H_2O and Cl^- with help of h_{VB}^+, $O_2^{\bullet-}$ and $^{\bullet}OH$

368 species.

369 **Scheme 1.**

370 **4. Conclusion**

371 In this study, we devised a novel heterostructure photocatalyst composed of Bi/SnO_2/TiO_2-G

372 that could efficiently photodegrade organic pollutants (here PCP). Upon visible light irradiation, the

373 photocatalyst could generate a large number of OH^- and $O_2^{\bullet-}$ reactive radicals, playing an important

374 role in PCP photodegradation. The excellent photocatalytic activity of the nanocomposite

375 photocatalyst is ascribed to its novel composition as well as its unique heterostructure. Taken

376 together, a promising, cost-effective, and highly efficient strategy has been introduced for the design

377 and synthesis of a novel visible light driven photocatalyst that can be used for the degradation of

378 organic contaminants in water treatment.

384

385 **Reference**

386 Ahmadpour N, Sayadi MH, Sobhani S, Hajiani M (2020) Photocatalytic degradation of model pharmaceutical
387 pollutant by novel magnetic TiO_2@$ZnFe_2O_4$/Pd nanocomposite with enhanced photocatalytic activity and
388 stability under solar light irradiation. Journal of Environmental Management 271: 110964
389 Alam U, Fleisch M, Kretschmer I, Bahnemann D, Muneer M (2017) One-step hydrothermal synthesis of Bi-
390 TiO_2 nanotube/graphene composites: An efficient photocatalyst for spectacular degradation of organic pollutants
391 under visible light irradiation Applied Catalysis B: Environmental 218:758-769
392 doi:https://doi.org/10.1016/j.apcatb.2017.06.016
393 Antonopoulou M, Vlastos D, Konstantinou I (2014) Photocatalytic degradation of pentachlorophenol by N-F-
394 TiO_2: Identification of intermediates, mechanism involved, genotoxicity and ecotoxicity evaluation Photochem
395 Photobiol Sci 14:520-527 doi:10.1039/C4PP00254G
396 Ba-Abbad MM, Takriff MS, Said M, Benamor A, Nasser MS, Mohammad AW (2017) Photocatalytic
397 Degradation of Pentachlorophenol Using ZnO Nanoparticles: Study of Intermediates and Toxicity International
398 Journal of Environmental Research 11:461-473 doi:10.1007/s41742-017-0041-3
399 Benjwal P, Kar KK (2015) One-step synthesis of Zn doped titania nanotubes and investigation of their visible
400 photocatalytic activity Materials Chemistry and Physics 160:279-288
401 doi:https://doi.org/10.1016/j.matchemphys.2015.04.038
402 Chen X, Mao SS (2007) Titanium Dioxide Nanomaterials: Synthesis, Properties, Modifications, and
403 Applications Chemical Reviews 107:2891-2959 doi:10.1021/cr0500535
404 Chen Z, Li Y, Guo M, Xu F, Wang P, Du Y, Na P (2016) One-pot synthesis of Mn-doped TiO_2 grown on
405 graphene and the mechanism for removal of Cr (VI) and Cr (III) Journal of hazardous materials 310:188-198

Elmolla ES, Chaudhuri M (2010) Degradation of amoxicillin, ampicillin and cloxacillin antibiotics in aqueous solution by the UV/ZnO photocatalytic process Journal of Hazardous Materials 173:445-449 doi:https://doi.org/10.1016/j.jhazmat.2009.08.104

Fujishima A, Honda K (1972) Electrochemical Photolysis of Water at a Semiconductor Electrode Nature 238:37-38 doi:10.1038/238037a0

Gaya UI, Abdullah AH (2008) Heterogeneous photocatalytic degradation of organic contaminants over titanium dioxide: A review of fundamentals, progress and problems Journal of Photochemistry and Photobiology C: Photochemistry Reviews 9:1-12 doi:https://doi.org/10.1016/j.jphotochemrev.2007.12.003

Ghadimi M, Zangenehtabar S, Homaeigohar S (2020) An Overview of the Water Remediation Potential of Nanomaterials and Their Ecotoxicological Impacts Water 12:1150

Gómez-Avilés A, Peñas-Garzón M, Bedia J, Rodriguez J, Belver C (2019) C-modified TiO2 using lignin as carbon precursor for the solar photocatalytic degradation of acetaminophen Chemical Engineering Journal 358:1574-1582

Grinberg VA et al. (2019) Photoelectrochemical Activity of Nanosized Titania, Doped with Bismuth and Lead, in Visible Light Region Protection of Metals and Physical Chemistry of Surfaces 55:55-64 doi:10.1134/S207020511901012X

Guo S, Wang H, Yang W, Fida H, You L, Zhou K (2020) Scalable synthesis of Ca-doped α-Fe$_2$O$_3$ with abundant oxygen vacancies for enhanced degradation of organic pollutants through peroxymonosulfate activation Applied Catalysis B: Environmental 262:118250 doi:https://doi.org/10.1016/j.apcatb.2019.118250

Habisreutinger SN, Schmidt-Mende L, Stolarczyk JK (2013) Photocatalytic Reduction of CO2 on TiO$_2$ and Other Semiconductors Angewandte Chemie International Edition 52:7372-7408 doi:10.1002/anie.201207199

Han R, Liu J, Chen N, Wang G, Guo Y, Wang H (2019) Synthesis of V-modified TiO$_2$ nanorod-aggregates by a facile microwave-assisted hydrothermal process and photocatalytic degradation towards PCP-Na under solar light. RSC Advances 9:34862-34871 doi:10.1039/C9RA05480D

Homaeigohar S (2020) The Nanosized Dye Adsorbents for Water Treatment Nanomaterials 10:295

Homaeigohar S, Botcha NK, Zarie ES, Elbahri M (2019) Ups and Downs of Water Photodecolorization by Nanocomposite Polymer Nanofibers Nanomaterials 9:250

Homaeigohar S, Davoudpour Y, Habibi Y, Elbahri M (2017) The Electrospun Ceramic Hollow Nanofibers Nanomaterials 7:383

Homaeigohar S, Elbahri M (2014) Nanocomposite Electrospun Nanofiber Membranes for Environmental Remediation Materials 7:1017-1045

Homaeigohar S, Strunskus T, Strobel J, Kienle L, Elbahri M (2018) A Flexible Oxygenated Carbographite Nanofilamentous Buckypaper as an Amphiphilic Membrane Advanced Materials Interfaces 5:1800001 doi:doi:10.1002/admi.201800001

Hosogi Y, Shimodaira Y, Kato H, Kobayashi H, Kudo A (2008) Role of Sn^{2+} in the Band Structure of SnM2O6 and Sn2M2O7(M = Nb and Ta) and Their Photocatalytic Properties Chemistry of Materials 20:1299-1307 doi:10.1021/cm071588c

Hu L et al. (2015) Facile synthesis of BiOF/Bi$_2$O$_3$/reduced graphene oxide photocatalyst with highly efficient and stable natural sunlight photocatalytic performance Journal of Alloys and Compounds 633:256-264 doi:10.1016/j.jallcom.2015.02.067

Hu M, Mi B (2013) Enabling graphene oxide nanosheets as water separation membranes Environmental science & technology 47:3715-3723

Jiang J, Zhang X, Sun P, Zhang L (2011) ZnO/BiOI Heterostructures: Photoinduced Charge-Transfer Property and Enhanced Visible-Light Photocatalytic Activity The Journal of Physical Chemistry C 115:20555-20564 doi:10.1021/jp205925z

Jiang W, Liu Y, Wang J, Zhang M, Luo W, Zhu Y (2016) Separation-free polyaniline/TiO$_2$ 3D hydrogel with high photocatalytic activity Advanced Materials Interfaces 3:1500502

Khan S et al. (2019) Exhaustive photocatalytic lindane degradation by combined simulated solar light-activated nanocrystalline TiO$_2$ and inorganic oxidants Catalysts 9:425

Kudo A, Miseki Y (2009) Heterogeneous photocatalyst materials for water splitting Chemical Society Reviews 38:253-278 doi:10.1039/B800489G

Kumar A, Rout L, Achary LSK, Mohanty A, Dhaka RS, Dash P (2016) An investigation into the solar light-driven enhanced photocatalytic properties of a graphene oxide–SnO$_2$–TiO$_2$ ternary nanocomposite RSC Advances 6:32074-32088 doi:10.1039/C6RA02067D

Kumar A, Rout L, Dhaka RS, Samal SL, Dash P (2015) Design of a graphene oxide-SnO$_2$ nanocomposite with superior catalytic efficiency for the synthesis of β-enaminones and β-enaminoesters RSC Advances 5:39193-39204 doi:10.1039/C5RA03363B

Kusiak-Nejman E, Morawski AW (2019) TiO$_2$/graphene-based nanocomposites for water treatment: A brief overview of charge carrier transfer, antimicrobial and photocatalytic performance Applied Catalysis B: Environmental 253:179-186 doi:https://doi.org/10.1016/j.apcatb.2019.04.055

Li D, Shi W (2016) Recent developments in visible-light photocatalytic degradation of antibiotics Chinese Journal of Catalysis 37:792-799 doi:10.1016/S1872-2067(15)61054-3

Liu Z, Wang Q, Tan X, Zheng S, Zhang H, Wang Y, Gao S (2020) Solvothermal preparation of Bi/Bi_2O_3 nanoparticles on TiO_2 NTs for the enhanced photoelectrocatalytic degradation of pollutants Journal of Alloys and Compounds 815:152478 doi:https://doi.org/10.1016/j.jallcom.2019.152478

Nguyen-Phan T-D, Pham VH, Chung JS, Chhowalla M, Asefa T, Kim W-J, Shin EW (2014) Photocatalytic performance of Sn-doped TiO_2/reduced graphene oxide composite materials Applied Catalysis A: General 473:21-30 doi:https://doi.org/10.1016/j.apcata.2013.12.030

Pourtaheri A, Nezamzadeh-Ejhieh A (2015) Photocatalytic properties of incorporated NiO onto clinoptilolite nano-particles in the photodegradation process of aqueous solution of cefixime pharmaceutical capsule Chemical Engineering Research and Design 104:835-843 doi:https://doi.org/10.1016/j.cherd.2015.10.031

Rajakumar G et al. (2014) Solanum trilobatum extract-mediated synthesis of titanium dioxide nanoparticles to control Pediculus humanus capitis, Hyalomma anatolicum anatolicum and Anopheles subpictus Parasitology Research 113:469-479 doi:10.1007/s00436-013-3676-9

Rajput H, Dhir A, Sangal V (2018) GO Mediated TiO_2 Nanotube Electrode for the Photoelectrocatalytic Degradation of Pentachlorophenol Journal of The Electrochemical Society 165:H16-H26 doi:10.1149/2.0871802jes

S.Sh. Homaeigohar, H. Mahdavi, Elbahri M (2012) Extraordinarily water permeable sol gel formed nanocomposite nanofibrous membranes Journal of Colloid and Interface Science 366:51-56

Sayadi MH, Sobhani S, Shekari H (2019) Photocatalytic degradation of azithromycin using $GO@Fe_3O_4/ZnO/SnO_2$ nanocomposites Journal of Cleaner Production 232:127-136 doi:https://doi.org/10.1016/j.jclepro.2019.05.338

Su Y et al. (2012) Two-Dimensional Carbon-Coated Graphene/Metal Oxide Hybrids for Enhanced Lithium Storage ACS nano 6:8349-8356 doi:10.1021/nn303091t

Tammina DSK, Mandal B, Ranjan S, Dasgupta N (2016) Cytotoxicity study of Piper nigrum seed mediated synthesized SnO_2 nanoparticles towards colorectal (HCT116) and lung cancer (A549) cell lines Journal of Photochemistry and Photobiology B: Biology 166 doi:10.1016/j.jphotobiol.2016.11.017

Tammina SK, Mandal BK, Ranjan S, Dasgupta N (2017) Cytotoxicity study of Piper nigrum seed mediated synthesized SnO2 nanoparticles towards colorectal (HCT116) and lung cancer (A549) cell lines Journal of Photochemistry and Photobiology B: Biology 166:158-168 doi:https://doi.org/10.1016/j.jphotobiol.2016.11.017

Tang Y, Wu D, Chen S, Zhang F, Jia J, Feng X (2013) Highly reversible and ultra-fast lithium storage in mesoporous graphene-based TiO_2/SnO_2 hybrid nanosheets Energy & Environmental Science 6:2447-2451 doi:10.1039/C3EE40759D

Wang C-Y, Zhang X, Qiu H-B, Huang G-X, Yu H-Q (2017) $Bi_{24}O_{31}Br_{10}$ nanosheets with controllable thickness for visible–light–driven catalytic degradation of tetracycline hydrochloride Applied Catalysis B: Environmental 205:615-623 doi:https://doi.org/10.1016/j.apcatb.2017.01.015

Wang P, Wang J, Wang X, Yu H, Yu J, Lei M, Wang Y (2013) One-step synthesis of easy-recycling TiO_2-rGO nanocomposite photocatalysts with enhanced photocatalytic activity Applied Catalysis B: Environmental 132-133:452-459 doi:https://doi.org/10.1016/j.apcatb.2012.12.009

Wu J, Qin F, Lu Z, Yang H-J, Chen R (2011) Solvothermal synthesis of uniform bismuth nanospheres using poly(N-vinyl-2-pyrrolidone) as a reducing agent Nanoscale Res Lett 6:66-66 doi:10.1186/1556-276X-6-66

Zhu M et al. (2018) Enhanced interfacial contact of dopamine bridged melamine-graphene/TiO_2 nano-capsules for efficient photocatalytic degradation of gaseous formaldehyde Applied Catalysis B: Environmental 232:182-193 doi:https://doi.org/10.1016/j.apcatb.2018.03.061
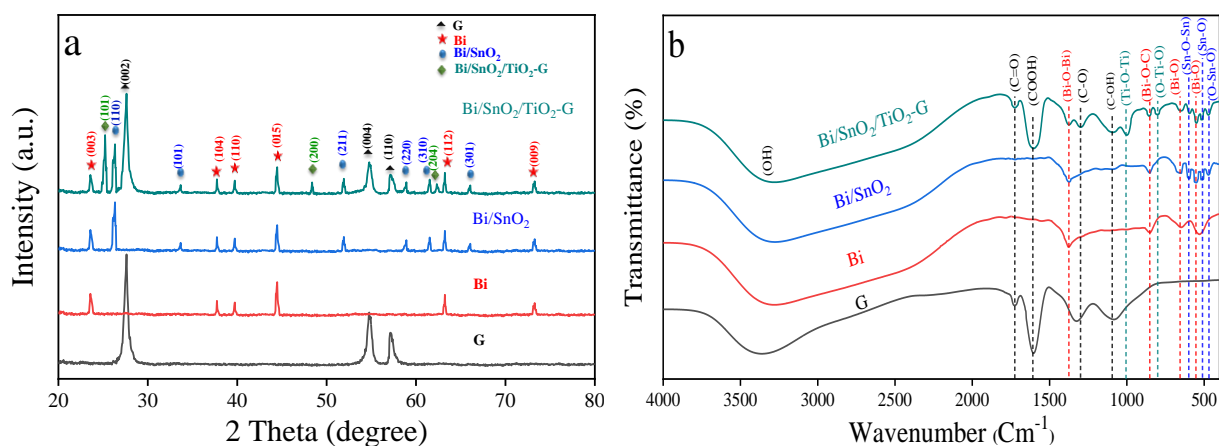
516

517

518

519

520

521

522

523

524

525

Table 1 The PCP photodegradation reaction rate constant with various types of the catalysts

| Catalyst	catalyst concentration (g/l)	PCP concentration (mg/l)	k (min^{-1})	R^2
Bi	0.3	20	0.007	0.9722
Bi/SnO$_2$	0.3	20	0.0101	0.9733
Bi/SnO$_2$/TiO$_2$-G	0.3	20	0.0149	0.9778

526

527

528

529

530

531

532

533

534

535

536

537

538
539 Figure 1. a) XRD and b) FTIR spectra for G, Bi, Bi/SnO₂ and Bi/SnO₂/TiO₂-G nanocomposite.
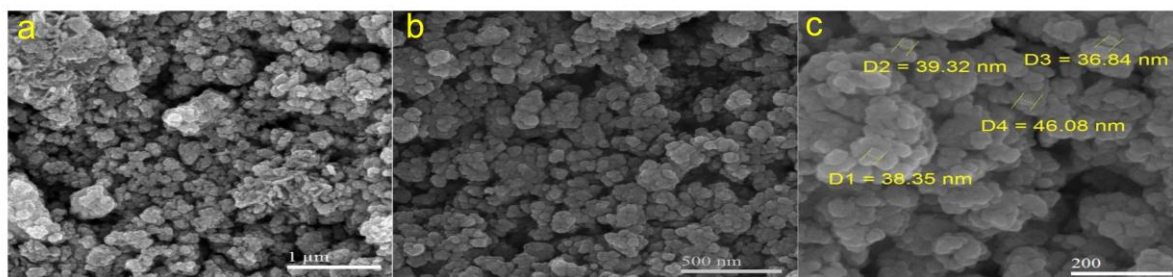
540
541 **Fig. 2.** SEM images of Bi/SnO₂/TiO₂-G photocatalyst particles at different magnifications (the scale bars represent 1µm (a),
542 500 nm (b), and 200 nm (c)). Note that the image shown in (c) presents approximate particle size of the synthesized
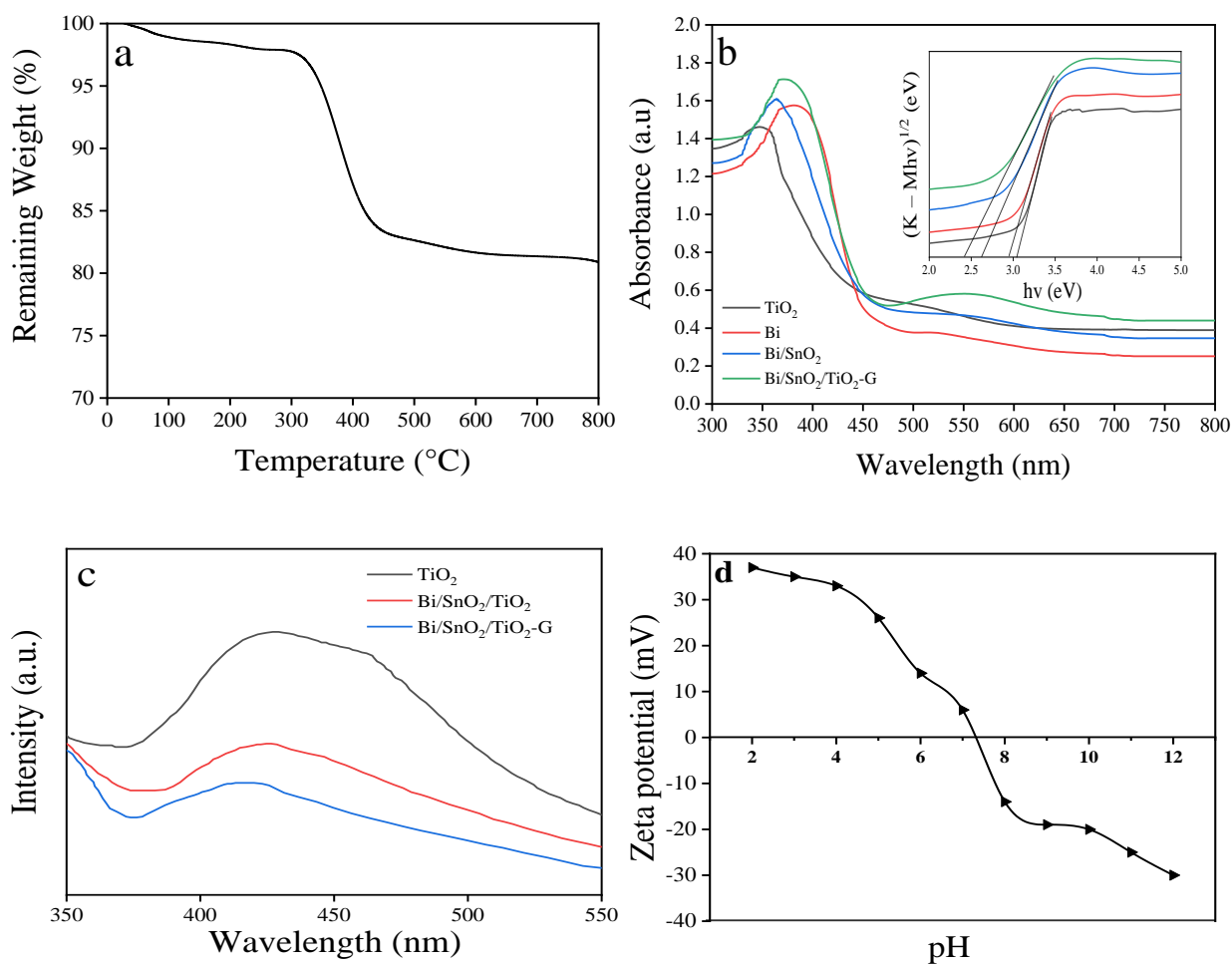543 photocatalyst particles.
544
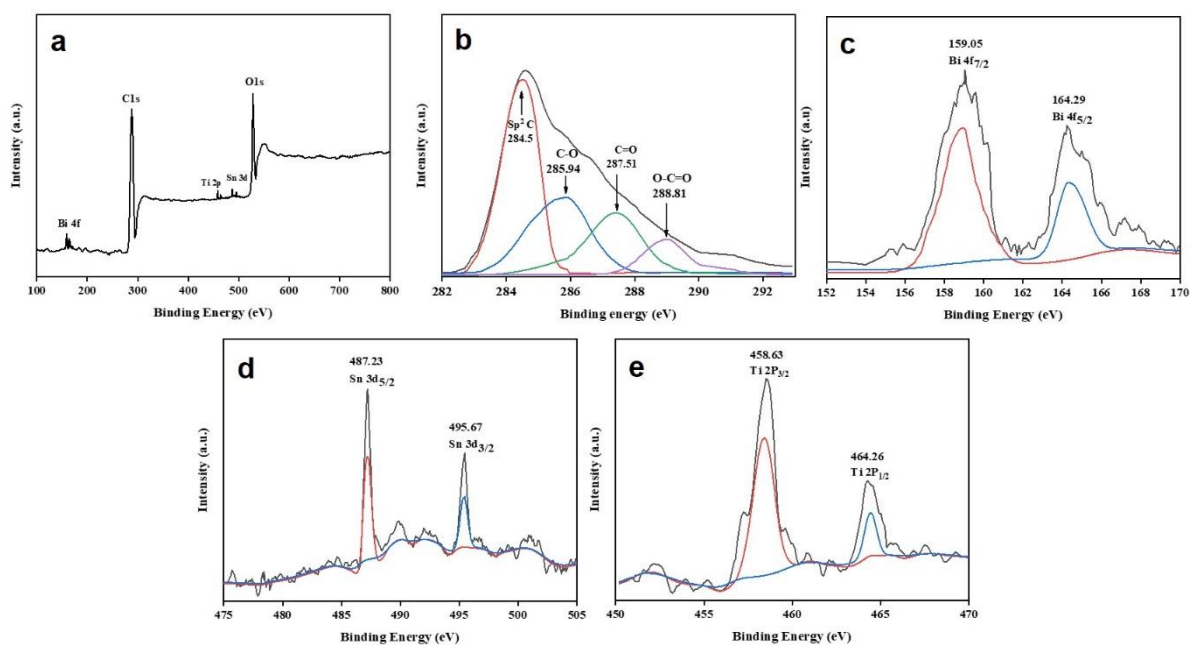
545
546 **Fig. 3.** XPS analysis of Bi/SnO₂/TiO₂-G nanocomposite: (a) general XPS spectrum of the compound; b) C1s; c) Bi 4f; d) Sn
547 3d; and e) Ti 2p spectrum.
548

549
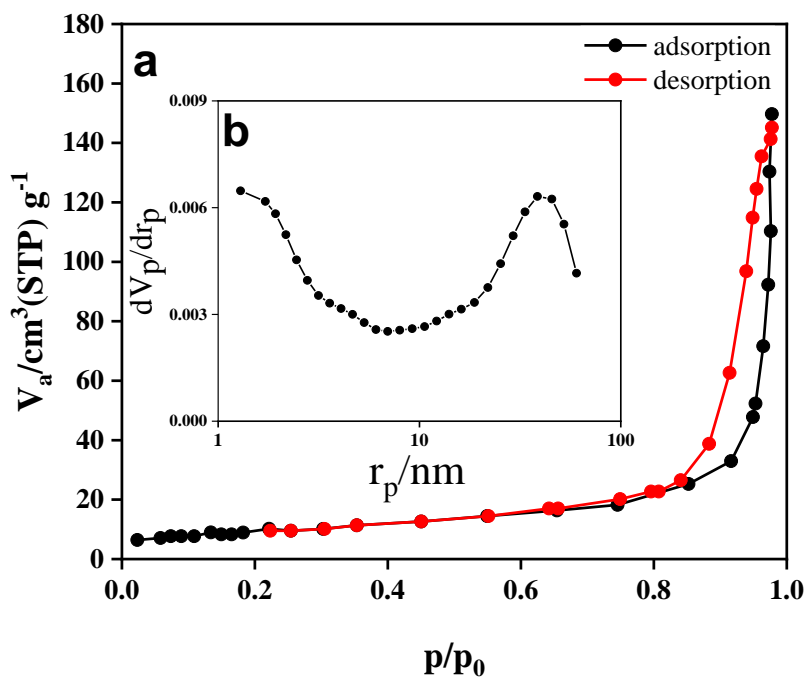
550
551 **Fig. 4.** N_2 adsorption-desorption isotherms of Bi/SnO$_2$/TiO$_2$-G nanocomposite. Inset pore size distributions from the
552 adsorption branch through the BJH method

553

Fig. 5. a) TGA spectrum for Bi/SnO$_2$/TiO$_2$-G; b) UV-visible absorption spectra for G, Bi-G, Bi/SnO$_2$-G and Bi/SnO$_2$/TiO$_2$-

555   G; c) PL spectra of the as-prepared pure TiO$_2$, Bi/SnO$_2$/TiO$_2$ and Bi/SnO$_2$/TiO$_2$-G samples. d) Zeta potential measurement

556   graph for Bi/SnO$_2$/TiO$_2$-G.

557
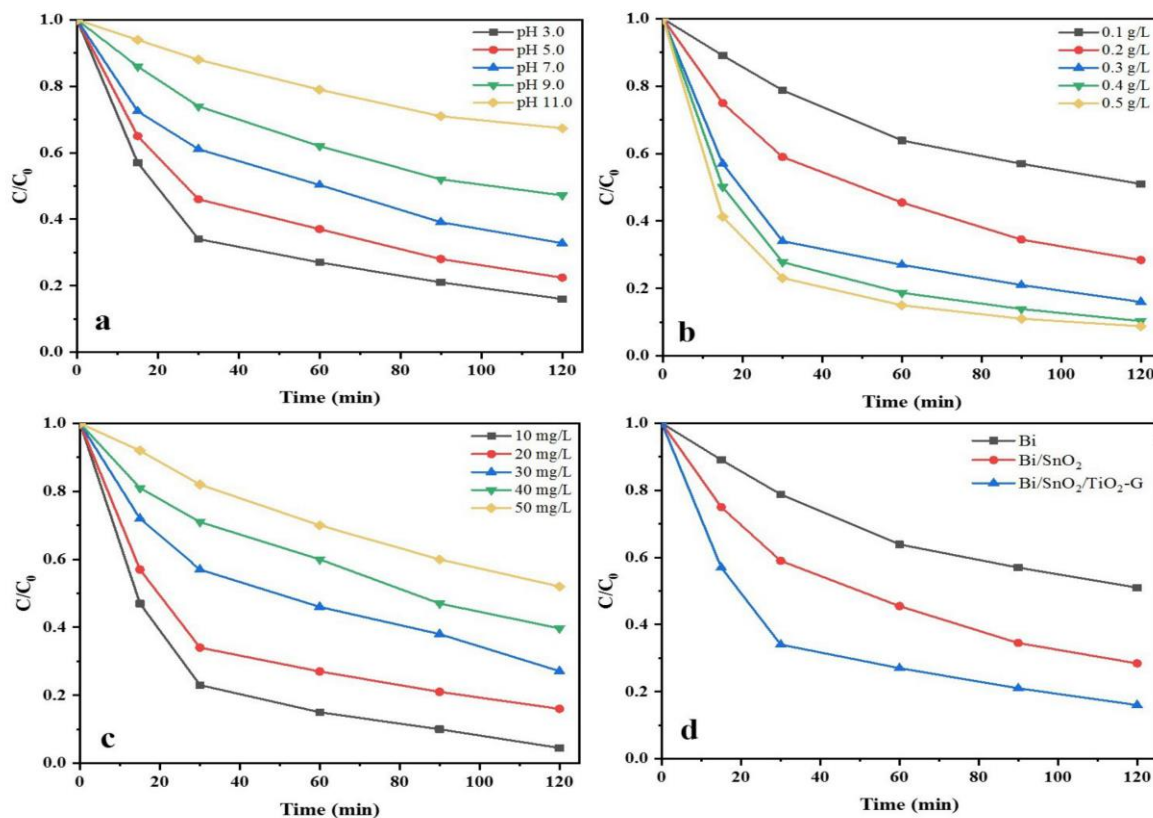
558
559   **Fig. 6.** The PCP photodegradation rate variations depending on a) pH; b) catalyst dose; c) PCP concentration; d) the catalyst
560   type.
561
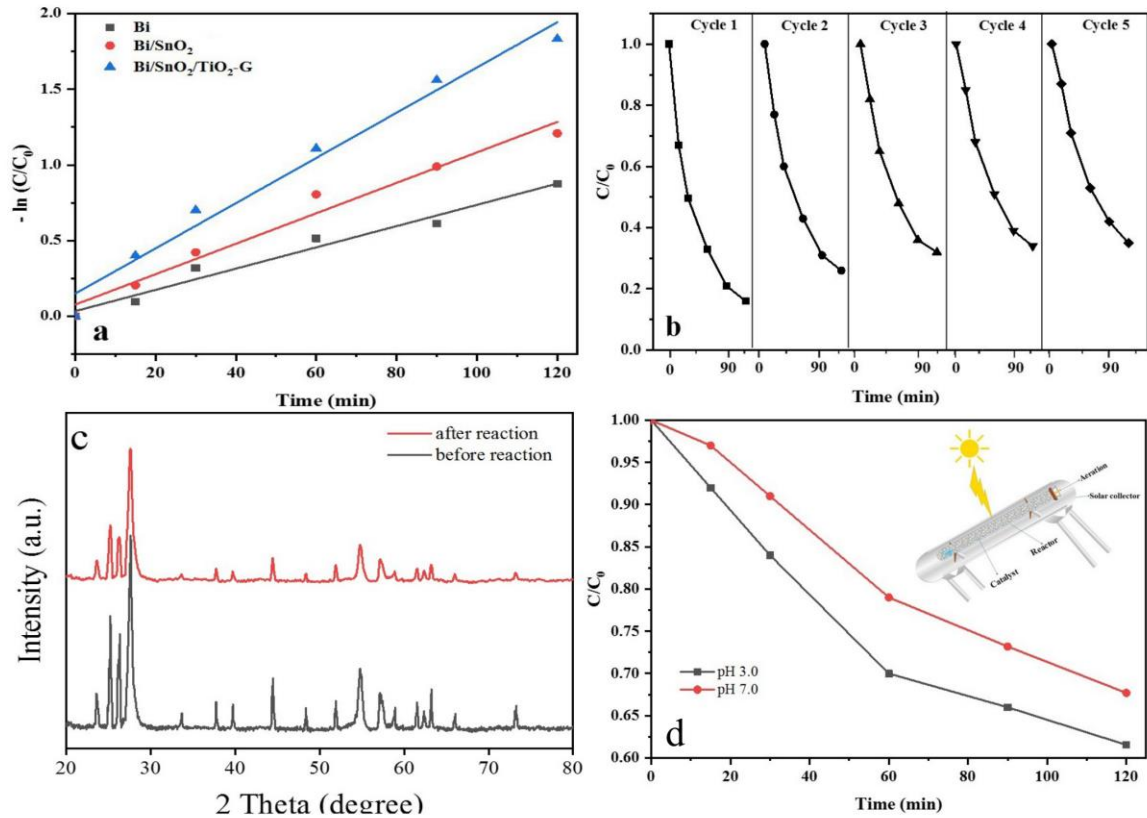
562
563 **Fig. 7.** a) Photodegradation kinetic behavior of the different photocatalysts; b) Reusability assessment for the Bi/SnO$_2$/TiO$_2$-
564 G photocatalyst in a cyclic manner; c) XRD pattern of Bi/SnO$_2$/TiO$_2$-G catalyst before and after 5 cycles. d) Visible light-
565 induced photodegradation of PCP under sunlight and different pHs.
566

567
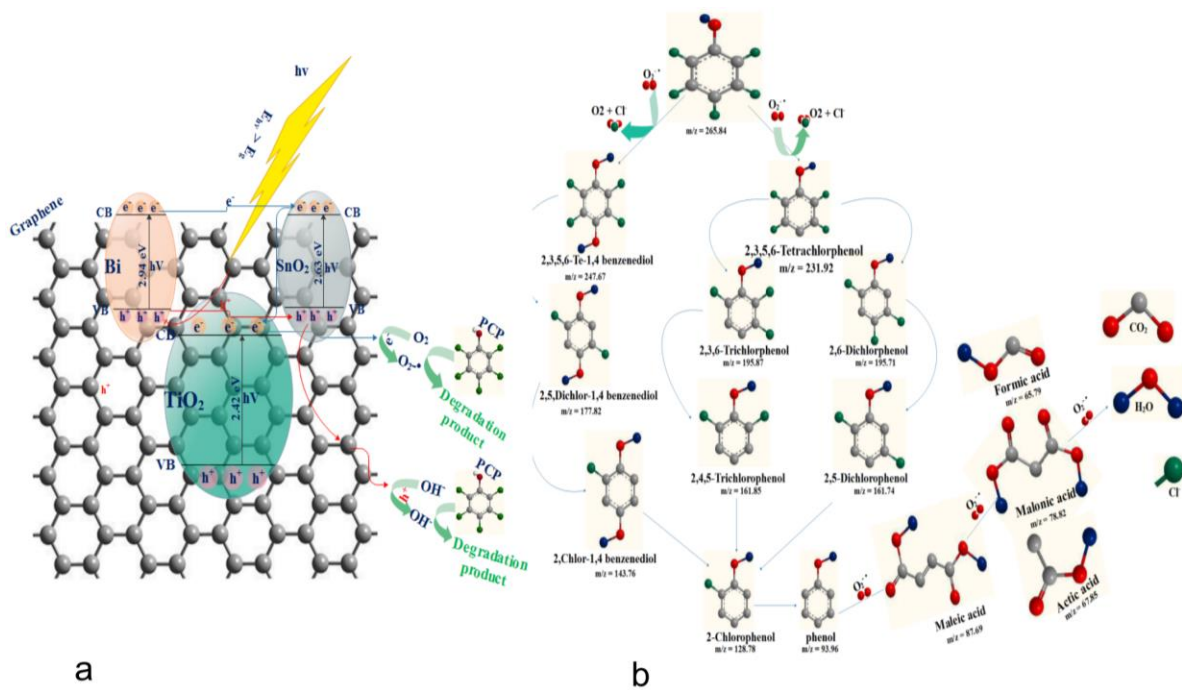
568 **Scheme 1.** a) The proposed mechanism for photocatalytic degradation of PCP by the Bi/SnO$_2$/TiO$_2$-G nanocomposite under
569 visible light irradiation. b) Possible reaction pathways of PCP degradation by the Bi/SnO$_2$/TiO$_2$-G nanocomposite.